Electromagnetic frozen waves with radial, azimuthal, linear, circular, and elliptical polarizations

Mateus Corato-Zanarella* and Michel Zamboni-Rached
School of Electrical and Computer Engineering, University of Campinas, Campinas, SP, Brazil
(Received 28 April 2016; revised manuscript received 1 September 2016; published 2 November 2016)

Frozen waves (FWs) are a class of diffraction- and attenuation-resistant beams whose intensity pattern along the direction of propagation can be chosen arbitrarily, thus making them relevant for engineering the spatial configuration of optical fields. To date, analyses of such beams have been done essentially for the scalar case, with the vectorial nature of the electromagnetic fields often neglected. Although it is expected that the field components keep the fundamental properties of the scalar FWs, a deeper understanding of their electromagnetic counterparts is mandatory in order to exploit their different possible polarization states. The purpose of this paper is to study the properties of electromagnetic FWs with radial, azimuthal, linear, circular, and elliptical polarizations under paraxial and nonparaxial regimes in nonabsorbing media. An intensity pattern is chosen for a scalar FW, and the vectorial solutions are built after it via the use of Maxwell's equations. The results show that the field components and the longitudinal component of the time-averaged Poynting vector closely follow the pattern chosen even under highly nonparaxial conditions, showing the robustness of the FW structure to parameters variations.

DOI: 10.1103/PhysRevA.94.053802

I. INTRODUCTION

The engineering of the spatial configuration of optical fields is of great interest in many areas, such as optical tweezers [1,2], atom guidance [3], and superresolution imaging [4–7]. In these cases, the transverse concentration and self-healing properties of Bessel beams (BBs) can be helpful, and frozen waves (FWs) provide an additional degree of freedom by allowing the modulation of the field intensity along the direction of propagation.

Currently, the theory of FWs allows the construction of diffraction- and attenuation-resistant beams with arbitrary intensity profile along the propagation axis in both nonabsorbing [8–13] and absorbing media [14–16]. Although "standard" FWs built with ideal BBs have infinite power flux, physically realizable alternatives can be constructed by truncating the BBs or by using Bessel-Gauss beams [16]. It has been shown both theoretically and experimentally that it is also possible to change the intensity profile of a FW over time [17].

Despite many advances in this field of research, the studies have generally adopted a scalar treatment, casting aside the vectorial characteristics of the electromagnetic fields. Although there are a few considerations for linearly polarized FWs under paraxial conditions [15], the analyses are far from being complete in this sense. In order to properly understand the characteristics of electromagnetic FWs and exploit their possible polarization states, a deeper study is required.

The goal of this paper is to analyze the properties of electromagnetic FWs with a variety of polarizations (radial, azimuthal, linear, circular, and elliptical) under paraxial and nonparaxial regimes in nonabsorbing media. Since the construction of FWs with finite power flux involves more complicated expressions, the present study focuses on the use of ideal BBs. Even though it is an idealization, the conclusions derived should be valid for practical FWs within the range in which their main composing BBs keep their localization properties.

*Corresponding author: mateuscorato@gmail.com

II. SCALAR FROZEN WAVES AND MATHEMATICAL METHODOLOGY

Throughout this paper, a time dependence of the form $e^{-i\omega t}$ is assumed for all the fields and, therefore, this factor will not be shown explicitly. For a summary of the theory of FWs in nonabsorbing media, the reader is referred to [8,9].

The vectorial solutions are constructed after a scalar FW (Ψ) of order ν propagating in the positive z direction. The desired intensity pattern, given by $|F(z)|^2$, is imprinted on a cylindrical surface of radius ρ_0 (for $\nu \neq 0$) or over the propagation axis with a spot radius $\Delta\rho_0$ (for $\nu = 0$) within the interval $0 \leqslant z \leqslant L$. Mathematically, it corresponds to $|\Psi(\rho = \rho_0, \phi, z)|^2 \approx |F(z)|^2$ for $\nu \neq 0$ and $|\Psi(\rho = 0, \phi, z)|^2 \approx |F(z)|^2$ for $\nu = 0$. The general form of Ψ is given by

$$\Psi(\rho,\phi,z) = \mathcal{N}_\nu \sum_{n=-N}^{N} A_n J_\nu(h_n \rho) e^{i\nu\phi} e^{i\beta_n z}, \tag{1}$$

where $\mathcal{N}_\nu = 1/[J_\nu(\cdot)]_{\max}$ (for which the same unit of Ψ is attributed) and $[J_\nu(\cdot)]_{\max}$ denotes the maximum value of the Bessel function of the first kind $J_\nu(\cdot)$. The coefficients A_n are calculated by

$$A_n = \frac{1}{L}\int_0^L F(z) e^{-i\frac{2\pi}{L}nz} dz. \tag{2}$$

The longitudinal (β_n) and transverse (h_n) wavenumbers are related by the expressions

$$\beta_n = Q + \frac{2\pi}{L}n, \quad h_n = \sqrt{k^2 - {\beta_n}^2}, \tag{3}$$

where $k = \overline{n}\omega/c$ (with c being the speed of light in vacuum) and $\overline{n}$ is the refractive index of the medium. They can also be expressed in terms of the cone angle of each BB (θ_n) by $\beta_n = k\cos\theta_n$ and $h_n = k\sin\theta_n$. In addition, Q is related to ρ_0 via the first solution of $\frac{\partial}{\partial\rho}[J_\nu(h_0\rho)]|_{\rho=\rho_0} = 0$ (or to $\Delta\rho_0$ via $\Delta\rho_0 \approx 2.4/h_0$ if $\nu = 0$), where $h_0 = \sqrt{k^2 - Q^2}$ according to Eq. (3). The maximum allowed value for N is

$$N_{\max} = \left\lfloor \frac{L}{2\pi} \min\{k - Q\,,\, Q\} \right\rfloor \tag{4}$$

so that $0 \leqslant \beta_n \leqslant k$, where $\lfloor\cdot\rfloor$ is the floor function.

The general procedure adopted is to choose a scalar FW as the desired transverse component of the electric field $\vec{E}$ and calculate its z component via Gauss's law (for source-free homogeneous media, it is $\vec{\nabla}\cdot\vec{E}=0$). The magnetic field is then obtained using Faraday's law ($\vec{B}=-\frac{i}{\omega}\vec{\nabla}\times\vec{E}$), and the time-averaged Poynting vector is calculated from the fields using $\vec{S}=\frac{1}{2\mu}\mathrm{Re}[\vec{E}\times\vec{B}^{*}]$, where μ is the magnetic permeability of the medium and $*$ denotes the complex conjugate.

III. CASES OF INTEREST

In certain cases, it is possible to simplify the expressions for the fields based on the values of the parameters Q and L. Let them be expressed by

$$Q=ak,\quad 0<a<1, \tag{5}$$

$$L=b\lambda,\quad b\in\mathbb{R}_{>0}. \tag{6}$$

Then, β_n can be written as

$$\beta_n=\beta_0\Big(1+\frac{n}{ab}\Big), \tag{7}$$

and $N_{\max}$ becomes $N_{\max}=\lfloor b\min\{1-a\,,a\}\rfloor$.

Since the maximum value for n is N, three main cases can be distinguished:

(1) $ab\gg N$ with $a\approx 1$: corresponds to the paraxial regime and is the most common case. Here, $\beta_n\approx\beta_0\approx k$, and $h_n\approx h_0\ll\beta_0$.

(2) $ab\gg N$ but with $a\not\approx 1$: corresponds to a nonparaxial situation in which the approximations $\beta_n\approx\beta_0$ and $h_n\approx h_0=k\sqrt{1-a^2}$ are still valid. Even so, this case can be highly nonparaxial, with h_0 even exceeding β_0 if $a<1/\sqrt{2}\approx 0.71$.

(3) $ab\not\gg N$ and $a\not\approx 1$: corresponds to a nonparaxial situation with very small L. In principle, taking the wavenumbers as being approximately constant is not a valid approximation in this case.

The approximate constancy of the wavenumbers in cases 1 and 2 allows multiplicative factors involving β_n and h_n to be taken outside summations, providing significant simplifications on the expressions of the fields and making their properties clearer. It is worth clarifying that these approximations are applied only to factors related to the amplitudes of the superposed BBs and should not be used on phase factors (like $e^{i\beta_n z}$).

IV. AZIMUTHAL POLARIZATION

If we write the vector wave equation for $\vec{E}$ [18] decomposed into cylindrical components and using cylindrical coordinates, that is, for $\vec{E}(\rho,\phi,z)=E_\rho\hat{\rho}+E_\phi\hat{\phi}+E_z\hat{z}$, we find that the resulting equations for E_ρ and E_ϕ are coupled. However, if we assume azimuthal symmetry [i.e., $\vec{E}(\rho,z)$], they become decoupled, and the equation for $E_\phi(\rho,z)$ turns out to be

$$\nabla^2E_\phi(\rho,z)-\frac{E_\phi(\rho,z)}{\rho^2}+k^2E_\phi(\rho,z)=0. \tag{8}$$

Since Eq. (8) is not the usual scalar wave equation [19], it is not possible to choose $E_\phi(\rho,z)$ as a scalar FW of arbitrary order. However, it is straightforward to verify that

$$E_\phi(\rho,z)=J_1(h\rho)e^{i\beta z}\hat{\phi},\quad \beta^2+h^2=k^2, \tag{9}$$

is a valid solution of Eq. (8), which is exactly a scalar BB of order $\nu=1$ without the exponential phase factor $e^{i\phi}$. Also, if we take $\vec{E}(\rho,z)=E_\phi(\rho,z)\hat{\phi}$, no other electric field components are necessary because $\vec{E}$ already satisfies Gauss's law due to the absence of ϕ dependence on E_ϕ, allowing us to take $E_\rho=E_z=0$.

So, since the missing exponential phase factor does not affect the intensity of the resulting field, we can build a FW with azimuthal polarization of the form

$$\vec{E}=E_\phi\hat{\phi},\quad E_\phi=\mathcal{N}_1\sum_{n=-N}^{N}A_nJ_1(h_n\rho)e^{i\beta_n z}. \tag{10}$$

The corresponding magnetic field is

$$\vec{B}=B_\rho\hat{\rho}+B_z\hat{z}, \tag{11}$$

$$B_\rho=-\frac{1}{\omega}\mathcal{N}_1\sum_{n=-N}^{N}\beta_nA_nJ_1(h_n\rho)e^{i\beta_n z}, \tag{12}$$

$$B_z=-\frac{i}{\omega}\mathcal{N}_1\sum_{n=-N}^{N}h_nA_nJ_0(h_n\rho)e^{i\beta_n z}, \tag{13}$$

and the time-averaged Poynting vector results in

$$\vec{S}=S_\rho\hat{\rho}+S_z\hat{z}, \tag{14}$$

$$S_\rho=-\frac{{\mathcal{N}_1}^2}{2\mu\omega}\sum_{n=-N}^{N}\sum_{m=-N}^{N}h_mJ_1(h_n\rho)J_0(h_m\rho)\times\mathrm{Im}[A_nA_m^{*}e^{i(\beta_n-\beta_m)z}], \tag{15}$$

$$S_z=\frac{{\mathcal{N}_1}^2}{2\mu\omega}\sum_{n=-N}^{N}\sum_{m=-N}^{N}\beta_mJ_1(h_n\rho)J_1(h_m\rho)\times\mathrm{Re}[A_nA_m^{*}e^{i(\beta_n-\beta_m)z}]. \tag{16}$$

Defining

$$\Psi_{\mathrm{FW}}^0\equiv\mathcal{N}_1\sum_{n=-N}^{N}A_nJ_0(h_n\rho)e^{i\beta_n z}, \tag{17}$$

which resembles a FW of order $\nu=0$, the expressions for cases 1 and 2 can be simplified to

$$B_\rho\approx-\frac{\beta_0}{\omega}E_\phi=-\frac{a\overline{n}}{c}E_\phi, \tag{18}$$

$$B_z\approx-i\frac{h_0}{\omega}\Psi_{\mathrm{FW}}^0=-i\frac{\sqrt{1-a^2}\overline{n}}{c}\Psi_{\mathrm{FW}}^0, \tag{19}$$

$$S_\rho\approx-\frac{h_0}{2\mu\omega}\mathrm{Im}\big[E_\phi\Psi_{\mathrm{FW}}^{0*}\big]=-\frac{\sqrt{1-a^2}}{2\eta}\mathrm{Im}\big[E_\phi\Psi_{\mathrm{FW}}^{0*}\big], \tag{20}$$

$$S_z\approx\frac{\beta_0}{2\mu\omega}|E_\phi|^2=\frac{a}{2\eta}|E_\phi|^2, \tag{21}$$

where $\eta=\sqrt{\mu/\epsilon}$ is the intrinsic impedance of the medium.

Equations (18) and (19) show that the magnetic field components follow the same FW pattern as E_ϕ (with order $\nu=1$ in B_ρ and $\nu=0$ in B_z), while Eq. (21) shows that S_z is proportional to $|E_\phi|^2$ and thus also mimics the intensity

profile of E_ϕ. In contrast, according to Eq. (20), the pattern of S_ρ is different, and the interpretation of its behavior is not as immediate. Since the term $E_\phi \Psi_{\mathrm{FW}}^{0*}$ involves products of the form $J_0(\cdot)J_1(\cdot)$, we expect oscillations that decay asymptotically with $1/\rho$ in the transverse plane, but the longitudinal behavior is not evident. A detailed analysis is carried out in Sec. VIII B, where it is shown that $S_\rho(\rho_0,z)\hat{\rho}$ points inward when $|E_\phi|^2$ increases and outward when $|E_\phi|^2$ decreases because it brings and removes energy from the field in accordance with its intensity pattern variation.

V. RADIAL POLARIZATION

The radial polarization is readily addressed considering the duality of electric and magnetic fields. If $\vec{B}$ is chosen as an azimuthally polarized FW, $\vec{E}$ will be a radially polarized FW (although with an unavoidable nonzero E_z component). This allows us to write an electric field of the form

$$\vec{E} = E_\rho \hat{\rho} + E_z \hat{z}, \quad E_\rho = \mathcal{N}_1 \sum_{n=-N}^{N} A_n J_1(h_n\rho) e^{i\beta_n z}. \tag{22}$$

Because of the duality, the results are basically the same as the ones in Sec. IV, with the roles of $\vec{E}$ and $\vec{B}$ interchanged. The expressions for the fields are

$$E_z = i\mathcal{N}_1 \sum_{n=-N}^{N} \frac{h_n}{\beta_n} A_n J_0(h_n\rho) e^{i\beta_n z}, \tag{23}$$

$$\vec{B} = B_\phi \hat{\phi}, \quad B_\phi = \frac{k^2}{\omega}\mathcal{N}_1 \sum_{n=-N}^{N} \frac{1}{\beta_n} A_n J_1(h_n\rho) e^{i\beta_n z}, \tag{24}$$

and those for the $\vec{S}$ components are

$$\vec{S} = S_\rho \hat{\rho} + S_z \hat{z}, \tag{25}$$

$$S_\rho = \frac{{\mathcal{N}_1}^2 k^2}{2\mu\omega} \sum_{n=-N}^{N}\sum_{m=-N}^{N} \frac{h_n}{\beta_n\beta_m} J_0(h_n\rho)J_1(h_m\rho) \times \mathrm{Im}[A_n A_m^* e^{i(\beta_n-\beta_m)z}], \tag{26}$$

$$S_z = \frac{{\mathcal{N}_1}^2 k^2}{2\mu\omega} \sum_{n=-N}^{N}\sum_{m=-N}^{N} \frac{1}{\beta_m} J_1(h_n\rho)J_1(h_m\rho) \times \mathrm{Re}[A_n A_m^* e^{i(\beta_n-\beta_m)z}]. \tag{27}$$

For cases 1 and 2, the approximations result in

$$B_\phi \approx \frac{k^2}{\omega\beta_0} E_\rho = \frac{\overline{n}}{ac} E_\rho, \tag{28}$$

$$E_z \approx i\frac{h_0}{\beta_0}\Psi_{\mathrm{FW}}^0 = i\frac{\sqrt{1-a^2}}{a}\Psi_{\mathrm{FW}}^0, \tag{29}$$

$$S_\rho \approx -\frac{k^2 h_0}{2\mu\omega{\beta_0}^2}\mathrm{Im}\left[E_\rho \Psi_{\mathrm{FW}}^{0*}\right] = -\frac{\sqrt{1-a^2}}{2\eta a^2}\mathrm{Im}\left[E_\rho \Psi_{\mathrm{FW}}^{0*}\right], \tag{30}$$

$$S_z \approx \frac{k^2}{2\mu\omega\beta_0}|E_\rho|^2 = \frac{1}{2\eta a}|E_\rho|^2. \tag{31}$$

As expected from the duality, the approximate expressions are also very similar to the ones found in Sec. IV.

VI. LINEAR POLARIZATION

Since each Cartesian component of the electric field obeys a scalar wave equation, it is possible to choose one of them as a scalar FW of arbitrary order. So, we can assume a linearly polarized $\vec{E}$ in the $\hat{x}$ or $\hat{y}$ direction of the form

$$\vec{E} = E_\perp \begin{pmatrix} \hat{x} \\ \hat{y} \end{pmatrix} + E_z \hat{z}, \tag{32}$$

$$E_\perp = \mathcal{N}_\nu \sum_{n=-N}^{N} A_n J_\nu(h_n\rho) e^{i\nu\phi} e^{i\beta_n z}, \tag{33}$$

where the bracket notation will be used to distinguish the terms corresponding to each direction chosen.

From now on, it is convenient to adopt the shorthand notation $J_\nu \equiv J_\nu(h_n\rho)$. Then, the expressions for the field components result in

$$E_z = \mathcal{N}_\nu \sum_{n=-N}^{N} A_n e^{i\beta_n z} e^{i\nu\phi} \left[\begin{pmatrix} \sin\phi \\ -\cos\phi \end{pmatrix} \frac{\nu}{\rho\beta_n} J_\nu + \frac{(J_{\nu-1} - J_{\nu+1})}{2} i \begin{pmatrix} \cos\phi \\ \sin\phi \end{pmatrix} \frac{h_n}{\beta_n} \right], \tag{34}$$

$$B_{\binom{x}{y}} = \frac{1}{\omega}\mathcal{N}_\nu \sum_{n=-N}^{N} A_n e^{i\beta_n z} e^{i\nu\phi} \begin{pmatrix} 1 \\ -1 \end{pmatrix} \left[\left(-\frac{i\nu\cos(2\phi)}{\rho^2\beta_n} + \frac{\nu^2\sin(2\phi)}{2\rho^2\beta_n} - \frac{{h_n}^2}{4\beta_n}\sin(2\phi) \right) J_\nu \right.$$
$$\left. + \frac{(J_{\nu-1} - J_{\nu+1})}{4\rho}\frac{h_n}{\beta_n}\left[2i\nu\cos(2\phi) - \sin(2\phi)\right] + \frac{(J_{\nu-2} + J_{\nu+2})}{8}\frac{h_n^2}{\beta_n}\sin(2\phi) \right], \tag{35}$$

$$B_{\binom{y}{x}} = \frac{1}{\omega}\mathcal{N}_\nu \sum_{n=-N}^{N} A_n e^{i\beta_n z} e^{i\nu\phi} \left\{ \left[\begin{pmatrix} \cos^2\phi \\ -\sin^2\phi \end{pmatrix} \frac{h_n^2}{2\beta_n} + \begin{pmatrix} 1 \\ -1 \end{pmatrix} \beta_n - \begin{pmatrix} 1 \\ 1 \end{pmatrix} \frac{i\nu\sin(2\phi)}{\rho^2\beta_n} + \begin{pmatrix} \sin^2\phi \\ -\cos^2\phi \end{pmatrix} \frac{\nu^2}{\rho^2\beta_n} \right] J_\nu \right.$$
$$\left. + \frac{(J_{\nu-1} - J_{\nu+1})}{2\rho}\frac{h_n}{\beta_n}\left[\begin{pmatrix} 1 \\ 1 \end{pmatrix} i\nu\sin(2\phi) + \begin{pmatrix} -\sin^2\phi \\ \cos^2\phi \end{pmatrix} \right] + \frac{(J_{\nu-2} + J_{\nu+2})}{4}\frac{h_n^2}{\beta_n} \begin{pmatrix} -\cos^2\phi \\ \sin^2\phi \end{pmatrix} \right\}, \tag{36}$$

$$B_z = \frac{1}{\omega}\mathcal{N}_\nu \sum_{n=-N}^{N} A_n e^{i\beta_n z} e^{i\nu\phi} \left[-\begin{pmatrix} \cos\phi \\ \sin\phi \end{pmatrix} \frac{\nu}{\rho} J_\nu + \frac{(J_{\nu-1} - J_{\nu+1})}{2} i h_n \begin{pmatrix} \sin\phi \\ -\cos\phi \end{pmatrix} \right]. \tag{37}$$

The explicit expressions for the time-averaged Poynting vector in terms of Bessel functions would be lengthy and of no much use.

In this polarization, the approximations for cases 1 and 2 must be done carefully. First, all the fields have terms with sine and cosine dependencies, so we have to keep the most significant one(s) of each type. Otherwise, the approximation would be poor. Second, $k = \bar{n}\omega/c$ is usually very high in optics (due to the high frequencies), and so are h_n and β_n. As a consequence, ${h_n}^2/\beta_n \overset{N}{\gg} h_n/\beta_n$, and $h_n/\beta_n \overset{N}{\gg} 1/\beta_n$ [20]. Third, the relative importance of the terms with ${h_n}^2/\beta_n$ and the one with β_n in Eq. (36) depends on the ratio h_n/β_n, which defines the regime (paraxial or nonparaxial). Since the β_n term does not depend on ϕ, it is not necessary to take one sine term and one cosine term when it is dominant. Taking all this into account, the approximate expressions become

$$E_z \approx \begin{pmatrix} \sin\phi \\ -\cos\phi \end{pmatrix} \frac{\nu}{\rho\beta_0} E_\perp + i \begin{pmatrix} \cos\phi \\ \sin\phi \end{pmatrix} \frac{h_0}{\beta_0} \Psi_{\mathrm{FW}}^{\nu\pm1}, \tag{38}$$

$$B_{\binom{x}{y}} \approx \begin{pmatrix} 1 \\ -1 \end{pmatrix} \left[-\frac{{h_0}^2}{\beta_0} \frac{\sin(2\phi)}{4\omega} \left(E_\perp - \Psi_{\mathrm{FW}}^{\nu\pm2} \right) + i \frac{h_0}{\beta_0} \frac{\nu \cos(2\phi)}{\omega\rho} \Psi_{\mathrm{FW}}^{\nu\pm1} \right], \tag{39}$$

$$B_{\binom{y}{x}} \approx \begin{cases} \begin{pmatrix} 1 \\ -1 \end{pmatrix} \frac{\beta_0}{\omega} E_\perp = \frac{a\bar{n}}{c} E_\perp \ \text{for case 1}, \\ \begin{pmatrix} 1 \\ -1 \end{pmatrix} \frac{\beta_0}{\omega} E_\perp + \begin{pmatrix} \cos^2\phi \\ -\sin^2\phi \end{pmatrix} \frac{{h_0}^2}{2\omega\beta_0} \left(E_\perp - \Psi_{\mathrm{FW}}^{\nu\pm2} \right) + \left[\begin{pmatrix} 1 \\ 1 \end{pmatrix} i\nu \sin(2\phi) + \begin{pmatrix} -\sin^2\phi \\ \cos^2\phi \end{pmatrix} \right] \frac{h_0}{\omega\rho\beta_0} \Psi_{\mathrm{FW}}^{\nu\pm1} \ \text{for case 2}, \end{cases} \tag{40}$$

$$B_z \approx -\begin{pmatrix} \cos\phi \\ \sin\phi \end{pmatrix} \frac{\nu}{\omega\rho} E_\perp + i \frac{h_0}{\omega} \begin{pmatrix} \sin\phi \\ -\cos\phi \end{pmatrix} \Psi_{\mathrm{FW}}^{\nu\pm1}, \tag{41}$$

where

$$\Psi_{\mathrm{FW}}^{\nu\pm1} \equiv \mathcal{N}_\nu \sum_{n=-N}^{N} A_n e^{i\beta_n z} e^{i\nu\phi} \frac{(J_{\nu-1} - J_{\nu+1})}{2}, \tag{42}$$

$$\Psi_{\mathrm{FW}}^{\nu\pm2} \equiv \mathcal{N}_\nu \sum_{n=-N}^{N} A_n e^{i\beta_n z} e^{i\nu\phi} \frac{(J_{\nu-2} + J_{\nu+2})}{2}. \tag{43}$$

The definitions in Eqs. (42) and (43) are motivated by the fact that the sum and the difference of Bessel functions that appear in them have characteristics similar to a Bessel function, i.e., they oscillate and decay, as illustrated in Fig. 1 for $\nu = 2$. Therefore, $\Psi_{\mathrm{FW}}^{\nu\pm1}$ and $\Psi_{\mathrm{FW}}^{\nu\pm2}$ have a transverse localization similar to that of a usual FW.

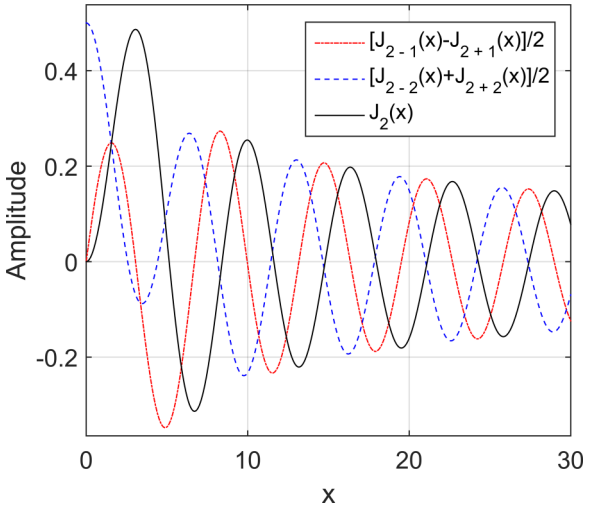

FIG. 1. Comparison among $J_\nu(x)$, $[J_{\nu-1}(x) - J_{\nu+1}(x)]/2$, and $[J_{\nu-2}(x) + J_{\nu+2}(x)]/2$ for $\nu = 2$, showing that they all oscillate and decay.

For case 1, since $\beta_0 \gg h_0$, it is clear from Eqs. (38) to (41) that $|E_z| \ll |E_\perp|$, $\left|B_{\binom{x}{y}}\right| \ll \left|B_{\binom{y}{x}}\right|$, and $|B_z| \ll \left|B_{\binom{y}{x}}\right|$, so the beam is almost TEM. It is also only in the paraxial case that the approximate expressions for the $\vec{S}$ components are simple because $B_{\binom{x}{y}}$ can be neglected when compared to $B_{\binom{y}{x}}$. Thus, considering $\vec{B} \approx B_{\binom{y}{x}}\binom{\hat{y}}{\hat{x}} + B_z\hat{z}$, we get

$$\vec{S} = S_\rho\hat{\rho} + S_\phi\hat{\phi} + S_z\hat{z}, \tag{44}$$

$$S_\rho \approx -\frac{h_0}{2\mu\omega} \mathrm{Im}\left[E_\perp \Psi_{\mathrm{FW}}^{\nu\pm1*} \right] = -\frac{\sqrt{1-a^2}}{2\eta} \mathrm{Im}\left[E_\perp \Psi_{\mathrm{FW}}^{\nu\pm1*} \right], \tag{45}$$

$$S_\phi \approx \frac{\nu}{2\mu\omega\rho} |E_\perp|^2 = \frac{\nu}{2\eta k\rho} |E_\perp|^2, \tag{46}$$

$$S_z \approx \frac{\beta_0}{2\mu\omega} |E_\perp|^2 = \frac{a}{2\eta} |E_\perp|^2. \tag{47}$$

It is worth noting that S_ϕ is proportional to ν and expresses the transverse energy circulation that gives rise to the orbital angular momentum (OAM) carried by the beam, which is an optical vortex beam with phase factor $e^{i\nu\phi}$. This fact also implies that the $\vec{S}$ field lines are helical [21,22].

VII. ELLIPTICAL AND CIRCULAR POLARIZATIONS

An elliptically polarized FW can be obtained by superposing two linearly polarized FWs in the $\hat{x}$ and $\hat{y}$ directions with a phase delay of $\pm\pi/2$ rad between them. In this case, $\vec{E}$ is

given by

$$\vec{E} = (u\hat{x} \pm iw\hat{y})E_{\perp} + E_z\hat{z}, \tag{48}$$

with $E_{\perp}$ taken from Eq. (33). u and w refer to the semiaxes of the ellipse in the $\hat{x}$ and $\hat{y}$ directions, respectively, and the plus and minus signs refer to right-hand and left-hand polarizations, respectively. If $u = w$, the field is circularly polarized.

The expressions for the fields components can be obtained by combining the results of Sec. VI, from which $\vec{S}$ can then be derived. It is also possible to assign different FWs to E_x and E_y, but the resultant wave would not be an elliptically polarized FW.

VIII. SIMULATIONS AND FURTHER DISCUSSION

Here, we focus on some aspects of experimentally feasible examples of cases 1 and 2 using visible light of wavelength $\lambda = 632.8\,\text{nm}$ propagating in air. Case 3, on the other hand, is analyzed separately in Sec. VIII F. For the two cases mentioned, the parameters used were as follows:

(1) Case 1 (paraxial): $N = 30$, $a = 0.9999$, and $b = 5.5310 \times 10^5$, implying $\beta_0 \approx 9.9282 \times 10^6\,\text{rad/m}$, $h_0 \approx 1.4042 \times 10^5\,\text{m}^{-1} \approx 0.0141\beta_0$, and $L = 0.35\,\text{m}$.

(2) Case 2 (nonparaxial): $N = 30$, $a = 0.7$, and $b = 1.5803 \times 10^4$, implying $\beta_0 \approx 6.9504 \times 10^6\,\text{rad/m}$, $h_0 \approx 7.0909 \times 10^6\,\text{m}^{-1} \approx 1.0202\beta_0$, and $L = 0.01\,\text{m}$.

The function $F(z)$ chosen for the simulations was

$$F(z) = \begin{cases} 1 & \text{for } 0.1L \leqslant z \leqslant 0.3L, \\ \sqrt{2} & \text{for } 0.4L \leqslant z \leqslant 0.6L, \\ \sqrt{3} & \text{for } 0.7L \leqslant z \leqslant 0.9L, \\ 0 & \text{otherwise,} \end{cases} \quad \text{within } 0 \leqslant z \leqslant L, \tag{49}$$

resulting in the intensity pattern $|F(z)|^2$ shown in Fig. 2 together with the obtained pattern for the superposition with $N = 30$. The unit of the electric field (and therefore of its intensity pattern $|\vec{E}|^2$) is arbitrary.

From now on, we denote $L_1 = 0.1L$ and $L_2 = 0.3L$, and the subscript $\perp$ refers to the transverse component of the fields. Since $|\vec{B}| = \overline{n}|\vec{E}|/c$ and $|\vec{S}| = |\vec{E}|^2/(2\eta)$ for a TEM wave and these same multiplicative factors appear in the approximate expressions of the fields, the plots of $\vec{B}$ and $\vec{S}$ will be of the form $c\vec{B}/\overline{n}$ and $2\eta\vec{S}$, so that these quantities follow the arbitrary unit of $|\vec{E}|$ and we avoid working with unnecessary powers of 10.

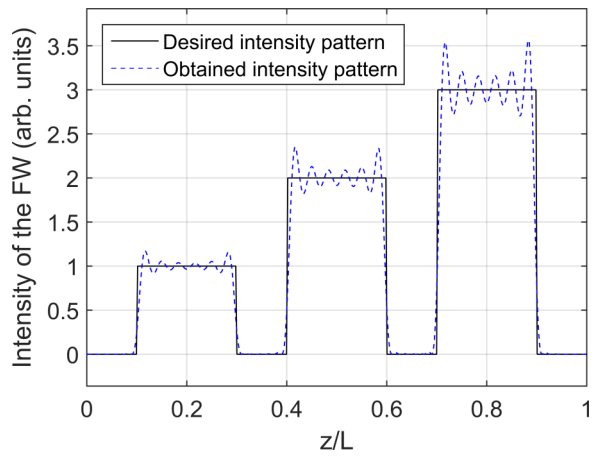

FIG. 2. Desired and obtained intensity patterns of the FW for $N = 30$, expressed in arbitrary units.

All the simulations were run with the complete field expressions, i.e., with no approximations.

A. Experimental feasibility, depth of penetration, and transverse spatial concentration

The feasibility of the cases chosen is related to the size of the apertures necessary to generate the BBs. The field depth Z of a BB truncated by a circular aperture of radius R can be approximated by $Z = R/\tan\theta$ [9], where θ is the cone angle. For a FW, it is sufficient that its composing BBs keep their localization properties inside the region in which the intensity is to be modeled (in this case, L). Since θ_n does not vary much around θ_0, we can estimate the necessary R by $R \approx L\tan\theta_0 = Lh_0/\beta_0$. This clearly shows the compromise between how much the FW is nonparaxial (characterized by the ratio h_0/β_0) and how far we want to model the field in order to achieve feasible apertures.

In the cases 1 and 2 chosen, we have $\theta_0 \approx 0.81^\circ$ and $\theta_0 \approx 45.57^\circ$, respectively, resulting in $R \approx 0.5\,\text{cm}$ and $R \approx 1.02\,\text{cm}$, which are perfectly realizable in laboratory. Even though case 2 is very nonparaxial and L is many orders of magnitude greater than λ, we still get a reasonable aperture size.

Regarding the spatial concentration, the more nonparaxial the BBs are, the higher h_0 is and, therefore, the smaller the spot or the radius of the FW is. Depending on the degree of nonparaxiality, we can have $\Delta\rho_0$ or ρ_0 of a fraction of λ (while still respecting the diffraction limit). For the parameters chosen in case 2, for example, we have $\Delta\rho_0 \approx 0.5349\lambda$ (for $\nu = 0$) and $\rho_0 \approx 0.4103\lambda$ (for $\nu = 1$). Hence, it should not be surprising that we can achieve details on the transverse intensity pattern of the beam that are smaller than the wavelength, as illustrated later in Fig. 6.

In practice, of course, a very concentrated transverse pattern requires a bigger aperture for a given propagation length, as highlighted above. Nevertheless, even for experimentally feasible apertures the depth of penetration of a FW can be many orders of magnitude higher than that of other usual beams. For example, a Gaussian beam with the same spot as the FW in case 2 has a Rayleigh length of $z_R = \pi\Delta\rho_0^2/\lambda \approx 0.9\lambda$ [23], which is much smaller than the $L \approx 1.5803 \times 10^4\lambda$ in which the FW keeps its transverse shape practically unaltered.

B. Azimuthal and radial polarizations

These are the simplest polarization cases, since the expressions for the fields have Bessel functions of only one order and present no ϕ dependence. The approximate expressions do not neglect any terms and hence are valid with extraordinary precision.

The transverse field components all follow the chosen FW pattern, and the longitudinal components are FWs of order zero with the same intensity variation in the z direction. As shown by the approximate expressions, the difference between

cases 1 and 2 is just an increase in the relative importance of the longitudinal components.

The most interesting analysis that can be made here regards the Poynting vector, since the same behavior appears in the other polarizations. Figure 3 shows the patterns of S_z and S_ρ for azimuthal polarization in case 1. For case 2, the shapes are the same, but with slightly different magnitudes.

As expected, S_z follows the pattern of $|E_\phi|^2$. It is worth mentioning that, although S_z is negligible near the propagation axis in the regions between the steps, there is no violation of energy conservation, which requires $\iint_{\mathbb{R}^2} S_z(x,y,z)\,dxdy = \text{const}$ [24]. What happens is that even though the total power flux through the transverse plane is constant, the regions in which the power flux density is concentrated change along the propagation direction due to the interference among the BBs composing the FW. As can be seen in Fig. 3(a), the magnitude of S_z at a certain distance from the axis increases in between the steps, so that the flux that was concentrated near it is now spread over a lateral structure, which extends beyond the limits of Fig. 3(a).

The behavior of S_ρ, on the other hand, is totally different: it is zero over the axis, increases suddenly, and then decays as ρ is increased, with ("inside" the steps of the pattern) or without (at the edges of the steps) changing sign along the radial direction.

A direct comparison of the sign of S_ρ over the radius of the FW (which can be seen in Fig. 4) with the longitudinal variation of the obtained pattern (Fig. 2) reveals that $S_\rho\hat{\rho}$ points outward when $|E_\phi|^2$ decreases and inward when it increases. The physical meaning of this fact is evident: S_ρ is responsible, at least in part, for the changes in the intensity of the fields and therefore has to bring or take away energy. Inside the steps, its magnitude is small because the intensity profile is almost flat, but it is much higher at the edges, where there are fast variations in $|E_\phi|^2$. As shown in Figs. 3(b) and 4, the "jumps" in the magnitude of S_ρ are proportional to the size of the steps, suggesting that they are somehow related to the derivative of $|E_\phi|^2$ with respect to z. This is also expected, because a greater change in the intensity pattern requires the transfer of more energy. For patterns with smooth variations, S_ρ remains small during the entire propagation, as verified via simulations with other $F(z)$.

The shape of S_ρ along the radial direction can be somewhat anticipated if we note that $E_\phi\Psi_{\text{FW}}^{0*}$ will be a sum of terms of the form $J_1(h_n\rho)J_0(h_m\rho)$ (among which h_n and h_m change only slightly) and that each of them oscillates and decays. However, at the edges of the steps, S_ρ does not change its sign radially like in the other positions, although it also decays.

C. Linear polarization

Unlike in the previous polarizations, the fields now have an azimuthal dependence, but for a fixed ϕ their components present the preassigned intensity pattern variation of the FW along the z direction, with a shape similar to the one shown in Fig. 3(a). In other words, the differences among the components lie entirely in their transverse patterns, which are modulated in the z direction by the chosen FW pattern. The radius (or spot) of the radial variation and the amplitude of the lateral rings for each of them depend on the order of the FW and on the value of ϕ. These considerations are also valid for the Poynting components besides S_ρ, whose characteristics will be analyzed separately.

In addition, the field expressions have many terms and involve Bessel functions of different orders. The terms also have disparate contributions to the total field, with some of them dependent on the ratio h_0/β_0. Because of this, when going from case 1 to 2, not only do the longitudinal fields get stronger, but there are also changes in the transverse patterns of some field components.

Because of all these facts, it is interesting to compare the different transverse profiles. Unless otherwise stated, the plots presented are for $z = (L_1 + L_2)/2$ and refer to a linearly polarized FW in the x direction with order $\nu = 2$.

As suggested by the approximate expressions of Sec. VI, E_z, B_z, and B_x keep the same kind of pattern when we change

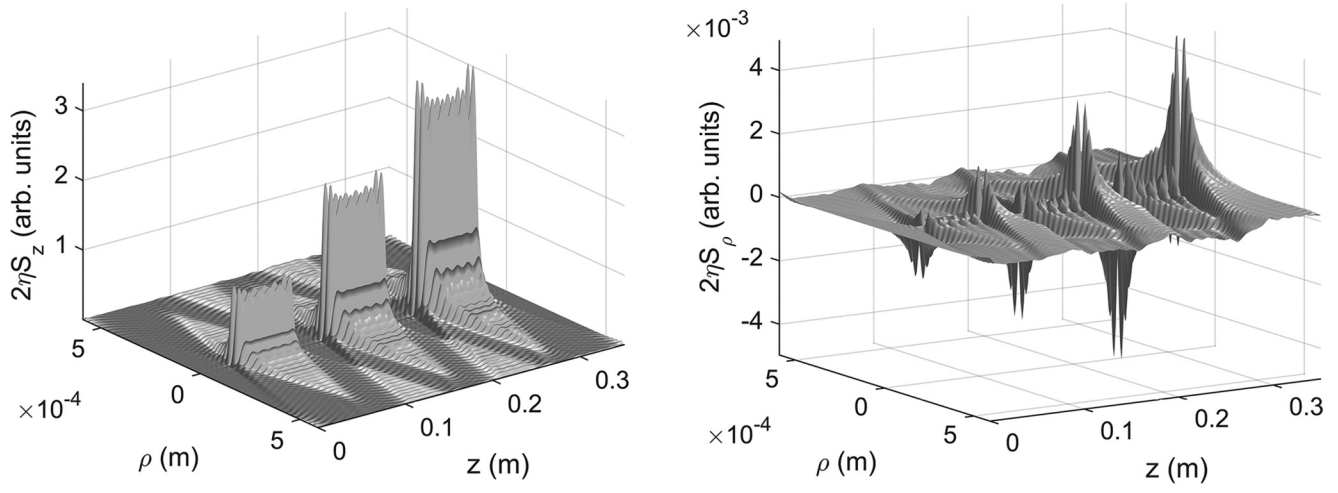

FIG. 3. Azimuthal polarization (case 1). Patterns of (a) S_z and (b) S_ρ along the z direction.

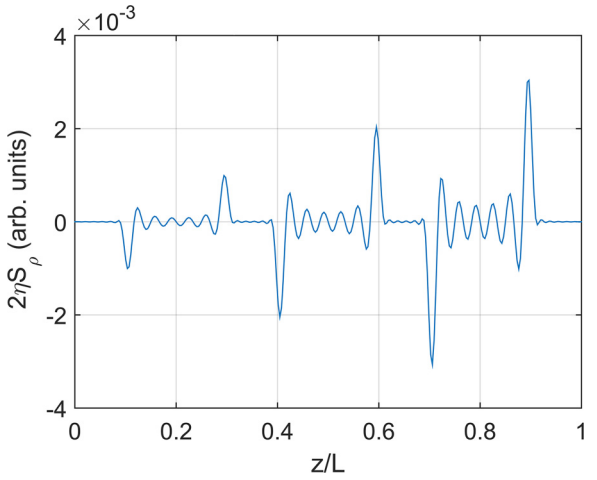

FIG. 4. Azimuthal polarization (case 1). $2\eta S_\rho$ evaluated at $\rho = \rho_0$ as a function of z.

from case 1 to 2, although their magnitudes increase because the ratio h_0/β_0 increases. Furthermore, E_z and B_z present the same pattern rotated by $\pi/2$ rad. Figure 5 illustrates the profiles of $|B_x|^2$ and $|B_z|^2$ for case 1, showing that, in agreement with the approximate expressions of Sec. VI, B_z has a superposition of $\cos\phi$ and $\sin\phi$ terms and B_x has a superposition of $\cos(2\phi)$ (decreasing with $1/\rho$) and $\sin(2\phi)$ terms.

On the other hand, the patterns of B_y and of the Poynting components are sensitive to the ratio h_0/β_0. To illustrate this fact, Fig. 6 shows what happens to $|B_y|^2$ and $|S_\phi|$ when we change from case 1 to case 2. In case 1, $|B_y|^2$ is proportional to $|E_\perp|^2$ (as are $|S_z|$ and $|S_\phi|$), but the term proportional to $h_0^2\cos^2\phi/\beta_0$ becomes more relevant when we change to case 2, making the field stronger over the x axis. As a result, $|S_\phi|$ (and also $|S_z|$, although it is not shown) is stretched in the x direction, following the change in B_y.

Comparing B_x and B_y in Figs. 5 and 6, we see that in case 1 $|B_x| \ll |B_y|$ and hence the magnetic field is linearly polarized. However, in case 2 (although not shown in Fig. 5) their magnitudes become comparable, and the polarization changes to elliptical.

The behavior of S_ρ is more peculiar. In case 1, the approximate Eq. (45) correctly indicates that it behaves as in Sec. VIII B. However, due to the nonparaxiality of case

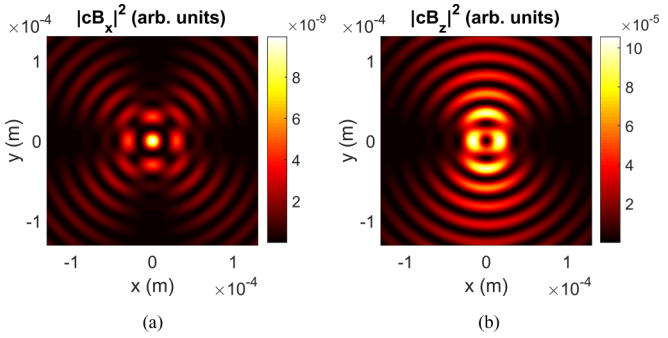

FIG. 5. Linear polarization (case 1). Patterns of (a) $|B_x|^2$ and (b) $|B_z|^2$ at $z = (L_1 + L_2)/2$.

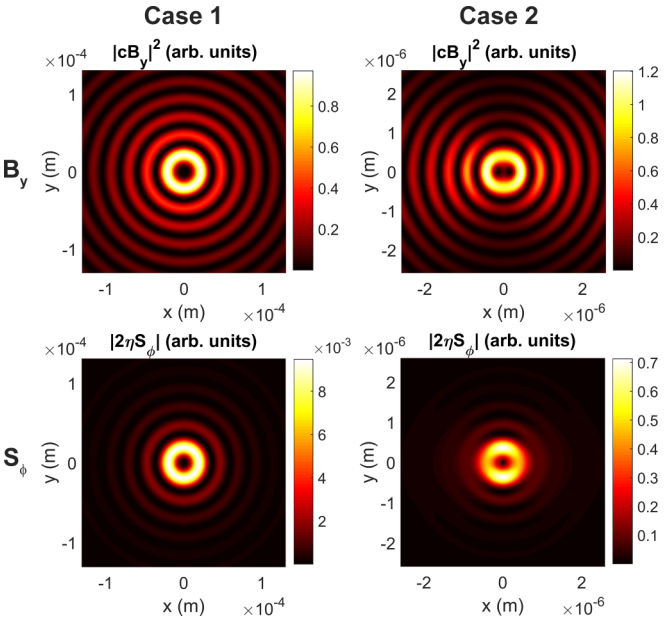

FIG. 6. Changes in the profiles of $|B_y|^2$ and $|S_\phi|$ at $z = (L_1 + L_2)/2$ incurred by the increase in the ratio h_0/β_0.

2, S_ρ starts to present different longitudinal behaviors for different values of ϕ. Figure 7 shows that for $\phi = \pi/4$ rad (and $\phi = 3\pi/4$ rad) it follows the FW pattern and points towards the propagation axis, but for $\phi = 0$ rad (and $\phi = \pi$ rad) it still behaves as in case 1. Although for the case presented the pattern in Fig. 7(a) is much less intense than the one in Fig. 7(b), their relative magnitudes depend strongly on the parameters Q and L and hence they could be comparable in other cases.

D. Elliptical and circular polarizations

Since the elliptical polarization is a combination of two linearly polarized waves, all the fields have the desired FW characteristics for a fixed ϕ, as in Sec. VIII C. To illustrate how the interaction between these two waves differs from a single linearly polarized FW, we will compare the results for a FW of order $\nu = 2$ with circular ($u = w = 1$) and elliptical ($u = 2$ and $w = 1$ chosen) polarizations with those of Sec. VIII C.

In case 1, E_x and E_y independently generate B_y and B_x, respectively, because the other contributions to these magnetic field components are negligible. Therefore, they have the same circular pattern of B_y in case 1 of Fig. 6 for both circular and elliptical polarizations. On the other hand, E_z and B_z receive comparable contributions from both E_x and E_y, and the final pattern depends on the values of u and w. As an illustration, Fig. 8 compares the profiles of $|E_z|^2$ in these two cases. For the circular polarization, the E_z components generated by E_x and E_y are in space quadrature and have the same magnitude, so they "close" a circle of intensity. For the elliptical polarization, the contribution from E_x is twice the one from E_y, resulting in an almost elliptical shape for $|E_z|^2$. The same conclusions are valid for B_z if the intensity pattern is rotated by $\pi/2$ rad.

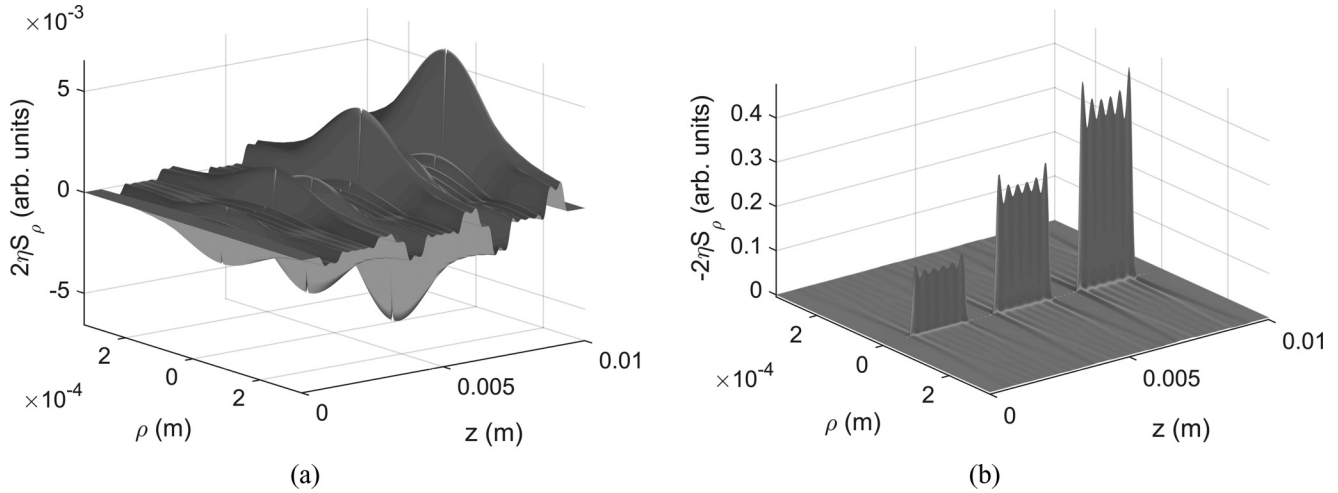

FIG. 7. Linear polarization (case 2). Longitudinal behavior of S_ρ for (a) $\phi = 0$ rad and $\phi = \pi$ rad and (b) $\phi = \pi/4$ rad and $\phi = 3\pi/4$ rad.

In respect to $\vec{S}$, S_ϕ and S_z have circular profiles similar to the ones in the left column of Fig. 6.

In case 2, the contributions for B_x due to E_x and for B_y due to E_y cannot be neglected, and their generation becomes intertwined. Also, the terms with azimuthal dependence become relatively more important and end up "stretching" the patterns of the resulting B_x and B_y in the same fashion as B_y in Fig. 6. This, of course, perturbs the circular symmetry of S_ϕ and S_z. As in the previous polarizations, the longitudinal fields also become stronger in case 2.

E. Approximations

A comparison of the exact results for azimuthal and radial polarizations with the ones obtained from approximate expressions shows that they agree precisely. For the linear and, consequently, elliptical or circular polarizations, the approximations for B_x, B_y, and $\vec{S}$ are less accurate due to the neglect of terms. Since these are less important under the paraxial regime, the approximations are precise for case 1. On the other hand, no terms are discarded in the approximations of E_z and B_z and, therefore, they are always very accurate.

In addition, the transverse characteristics of the fields components for all the polarization states are very similar to the ones obtained for single BBs [25,26], since the variations on h_n are small and the superposed BBs are therefore very similar.

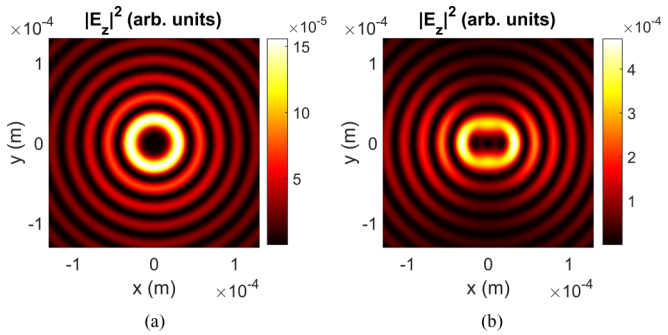

FIG. 8. Transverse pattern of $|E_z|^2$ in case 1 for (a) circular polarization and (b) elliptical polarization at $z = (L_1 + L_2)/2$.

F. Analysis of case 3

Although it does not seem possible, *a priori*, to make any approximation for case 3, it was noted that the fields obtained in such a case present practically the same transverse patterns and magnitudes as the ones that would be obtained in a case 2 with the same value of Q. This indicates that we can actually use the approximate expressions of case 2 for case 3 without losing precision. There are basically two facts that make this possible and they will be numerically illustrated for a case in which $a = 0.5$ and $b = 100$. Experimentally, this case would demand an aperture of radius $R \approx 0.11$ mm, which is totally feasible despite the extreme nonparaxiality.

First, the transverse pattern of the FW is determined by a superposition of the Bessel functions, whose maxima positions differ because h_n varies. However, if this deviation is small, even considerable changes in h_n do not alter the localized properties of the profile, which is actually what happens in most practical situations. For the case 3 chosen, Fig. 9(a) shows $J_2(h_n\rho)$ when h_n varies from h_0 to h_{-N} and h_N. The maximum deviation of the peak from the case with h_0 [which is the one in which the FW pattern is centered, as will be shown in Fig. 9(b)] occurs for $n = N$ and increases with the value of ν. However, unless ν is taken to be excessively high, the deviation is not enough to strongly separate the peaks and they still "interfere constructively." The superposition outside the peak is destructivelike, and the FW localization property is kept.

Second, the coefficients A_n are usually significant only near a certain value of n (which is usually $n = 0$), making the contributions of the terms with distant values of n almost negligible. Because of this, the "effective" maximum change in h_n that should be considered when analyzing the shift of the Bessel functions is smaller. For the case 3 chosen, for example, Fig. 9(b) exhibits the values of $|A_n|$ and shows that they are only significant near $n = 0$.

In conclusion, this shows that the localized structure of the FWs is very robust to parameters variations.

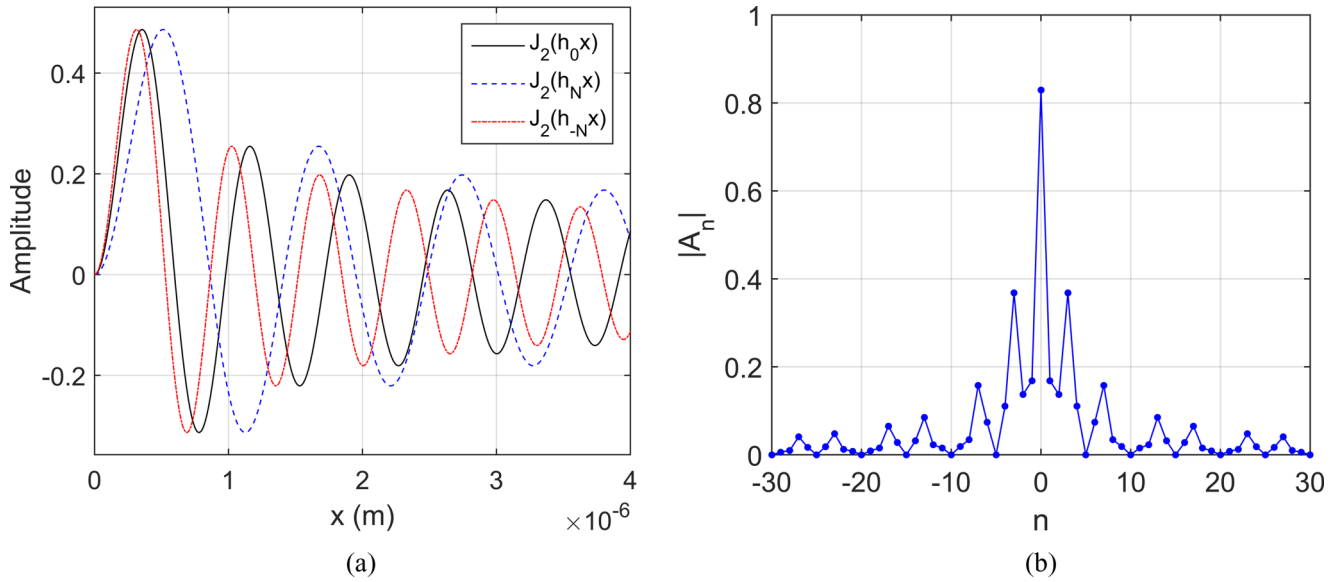

FIG. 9. Case 3. (a) Comparison among $J_2(h_n x)$ when h_n varies. (b) $|A_n|$ vs n.

IX. CONCLUSIONS

In this paper we presented a variety of possible polarization states for electromagnetic frozen waves and analyzed their characteristics for three distinct cases: the paraxial regime (case 1) and nonparaxial regimes with high (case 2) and low (case 3) field depths. The localization property of the scalar FWs is kept by all the fields and time-averaged Poynting components (except for the radial one, S_ρ), even when there are azimuthal dependencies on their expressions. For cases 1 and 2, the small variations on the transverse (h_n) and longitudinal (β_n) wavenumbers allow approximations that greatly simplify the analysis of the fields with almost no loss of precision. In addition, a study of case 3 shows that even in extreme cases the variations on h_n are not enough to break the localization properties of the FWs, which appear to be very robust structures in this sense. Furthermore, the approximate expressions for case 2 can generally still be used in these situations.

[1] L. A. Ambrosio and M. M. Ferreira, J. Opt. Soc. Am. B **32**, B67 (2015).
[2] V. Garcés-Chávez, D. McGloin, H. Melville, W. Sibbett, and K. Dholakia, Nature (London) **419**, 145 (2002).
[3] J. Arlt, T. Hitomi, and K. Dholakia, Appl. Phys. B **71**, 549 (2000).
[4] R. Merlin, Science **317**, 927 (2007).
[5] A. Grbic, L. Jiang, and R. Merlin, Science **320**, 511 (2008).
[6] E. Pastrana, Nat. Methods **10**, 102 (2013).
[7] W. Yu, Z. Ji, D. Dong, X. Yang, Y. Xiao, Q. Gong, P. Xi, and K. Shi, Laser Photonics Rev. **10**, 147 (2016).
[8] M. Zamboni-Rached, Opt. Express **12**, 4001 (2004).
[9] M. Zamboni-Rached, E. Recami, and H. E. Hernández-Figueroa, J. Opt. Soc. Am. A **22**, 2465 (2005).
[10] T. A. Vieira, M. R. R. Gesualdi, and M. Zamboni-Rached, Opt. Lett. **37**, 2034 (2012).
[11] T. A. Vieira, M. Zamboni-Rached, and M. R. Gesualdi, Opt. Commun. **315**, 374 (2014).
[12] I. Ouadghiri-Idrissi, R. Giust, L. Froehly, M. Jacquot, L. Furfaro, J. M. Dudley, and F. Courvoisier, Opt. Express **24**, 11495 (2016).
[13] T. Cizmar and K. Dholakia, Opt. Express **17**, 15558 (2009).
[14] M. Zamboni-Rached, Opt. Express **14**, 1804 (2006).
[15] M. Zamboni-Rached, L. A. Ambrósio, and H. E. Hernández-Figueroa, Appl. Opt. **49**, 5861 (2010).
[16] M. Zamboni-Rached and M. Mojahedi, Phys. Rev. A **92**, 043839 (2015).
[17] T. A. Vieira, M. R. R. Gesualdi, M. Zamboni-Rached, and E. Recami, Opt. Lett. **40**, 5834 (2015).
[18] $(\vec{\nabla} \times \vec{\nabla} \times -k^2)\vec{E} = \vec{0}$.
[19] $(\nabla^2 + k^2)\Psi = 0$.
[20] Here, $\overset{N}{\gg}$ means numerically much greater than.
[21] A. Bekshaev, K. Bliokh, and M. Soskin, J. Opt. **13**, 053001 (2011).
[22] A. Bekshaev, M. Soskin, and M. Vasnetsov, *Paraxial Light Beams with Angular Momentum* (Nova Science Publishers, New York, 2008).
[23] This is a conservative estimate because this Gaussian beam is so nonparaxial that its analytical expression, derived for the paraxial regime, should not be valid here. However, we expect that the more nonparaxial the beam is, the faster it diffracts.
[24] In order to write this, we must assume that the FW was generated with finite power flux, which can be achieved by truncating its composing BBs with an aperture, as exposed in Sec. VIII A. Otherwise, the integral would diverge.
[25] Y. Wang, W. Dou, and H. Meng, Opt. Express **22**, 7821 (2014).
[26] Y. Z. Yu and W. B. Dou, Prog. Electromagn. Res. Lett. **5**, 57 (2008).